

A Double Detector for RFI Mitigation in Microwave Radiometers

Jeffrey R. Piepmeier, *Member, IEEE*, Priscilla N. Mohammed, *Member, IEEE*, and Joseph J. Knuble

Abstract—A double detector (DD) for radio-frequency interference (RFI) in microwave radiometers is demonstrated in theory and practice. The detector is based on the principle of using kurtosis to detect the presence of non-Gaussian signals and is shown to approximate the kurtosis of input. Theoretical response to continuous wave and pulsed RFI is derived and tested in two experiments. The DD hardware comprises two microwave detectors, two integrator-amplifiers, and a wideband video amplifier. The technique is compatible with existing direct-detection radiometer designs and desirable for applications requiring low technological risk.

Index Terms—Kurtosis, radio-frequency interference (RFI), radiometer, signal detection.

I. INTRODUCTION

RADIO-FREQUENCY interference (RFI) can corrupt microwave radiometer measurements. Some striking examples include [2], [6], and [8]. High levels of RFI can cause measurements over specific regions to be simply unusable. Or perhaps worse, low-level RFI can create erroneous retrievals unknown to the user. Even when operating strictly within passive allocations—many of which are shared—radio regulations do *not* guarantee an RFI-free environment (ITU-R RS.1029). To date, RFI detection in spaceborne radiometers is done in postprocessing using image statistics and expected spectral or polarization characteristics of surface brightness temperatures [2], [8]. Hardware-based RFI detectors or mitigators are not yet used in space, although two digital RFI receivers have been demonstrated on aircraft [3], [10].

A simple hardware RFI detector for microwave radiometers is described in this paper. The double detector (DD) is based on the concept of using the kurtosis statistic as a non-Gaussian signal detector [10]. This was recently demonstrated by Ruf *et al.* using an intermediate frequency (IF) digital receiver that estimates the variance (proportional to brightness temperature) and kurtosis of a signal received by a radiometer. The DD described herein was conceived as a simple augmentation to a conventional direct-detection radiometer for measuring the signal's kurtosis statistic. The advanced digital RFI receiver of Ruf *et al.* requires a downconversion stage (local oscillator,

mixer, and IF amplifiers) for observing frequencies higher than 1 or 2 GHz, high-speed analog-to-digital converters (ADCs) sampling at a rate of 50–400 MHz (i.e., at Nyquist rate for the passband width), and digital processing logic. Although that architecture allows for advanced signal processing, it is not appropriate for use in risk-averse environments. The DD, on the other hand, uses as its first element a microwave detector already found in conventional direct-detection radiometers. Thus, additional downconversion hardware is not needed for observing up to ~40 GHz. In fact, there is no impact on the microwave design of the radiometer. The additional hardware comes in the video section after the detector. The outputs of the DD are sampled at conventional radiometer rates (e.g., 1 or 10 ms) so high-speed ADCs and onboard digital processing also are not needed. The purpose of the DD is to provide a detector that approximates the kurtosis statistic and can be added to radiometer designs with low technological risk and little impact to system resources. It is appropriate for missions requiring high-technology readiness-level solutions such as the National Polar-orbiting Operational Environmental Satellite System.

The design and use of the DD are described in this paper. Section II contains the mathematical basis of the DD. A discussion of hardware implementation and experiments, as well as the practical aspects of detector linearization, can be found in Section III. The paper concludes with a discussion in Section IV.

II. DOUBLE DETECTOR

Naturally occurring thermal emission and self-generated receiver noise measured by a radiometer are well modeled using Gaussian distributions. Interference-free Gaussian signals have a constant relationship between their power or the second central moment μ_2 and their fourth central moment μ_4 . This relationship is the kurtosis, which is defined as the ratio

$$\beta_2 = \frac{\mu_4}{\mu_2^2} \quad (1)$$

and is equal to three if the input is Gaussian. The deviation of this quotient from its constant value of three is an indicator of the presence of non-Gaussian RFI [10].

The microwave detector found in conventional direct-detection radiometer designs already measures the second central moment of the received signal. The DD was conceived to approximate the fourth central moment by augmenting the preexisting detector. As shown in Fig. 1, the received signal $x(t)$ is first input to a microwave detector. In direct-detection radiometers, $x(t)$ is centered at the RF, and in radiometers

Manuscript received February 18, 2007; revised July 15, 2007. This work was supported by the National Aeronautics and Space Administration Earth Science Technology Office.

J. R. Piepmeier and J. J. Knuble are with the Microwave Instrument Technology Branch, NASA Goddard Space Flight Center, Greenbelt, MD 20771 USA.

P. N. Mohammed is with the Microwave Instrument Technology Branch, NASA Goddard Space Flight Center, Greenbelt, MD 20771 USA, and also with the Goddard Earth Sciences and Technology Center, University of Maryland Baltimore County, Baltimore, MD 21250 USA.

Digital Object Identifier 10.1109/TGRS.2007.909099

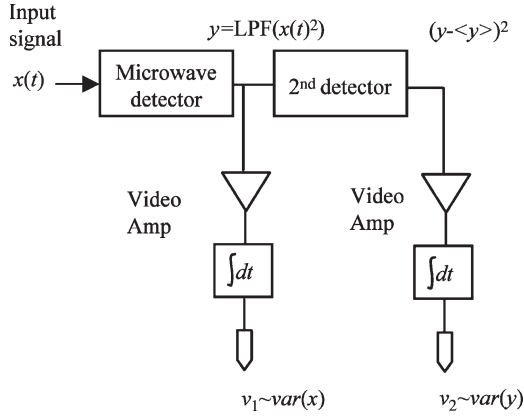


Fig. 1. Block diagram of double-detector system. The first detector is modeled as a square-law device that retains the baseband portion of the squared input. The second detector senses the power output from the first.

with downconversion, it is centered at the IF. The output of the first detector is a baseband video frequency (VF) signal $y(t)$, which is formed by taking only the baseband portion of $x^2(t)$, as indicated by the low-pass filter (LPF) operator. It is assumed that the first detector's video bandwidth is equal to or greater than the RF passband width B . The video amplifier produces output v_1 from the dc component of $y(t)$, which are both proportional to the power of $x(t)$. The second detector and video amplifier measures the power in the VF signal, which includes the fourth central moment of $x(t)$. Together, the two output voltages v_1 and v_2 can be used to approximate the kurtosis.

A. Pseudokurtosis With Gaussian Input

The pseudokurtosis ψ , which is an approximation of the true kurtosis β_2 , for the DD system shown in Fig. 1 is defined as

$$\psi \equiv \frac{\text{var}(y)}{\langle y \rangle^2} \quad (2)$$

where $y(t)$ is the baseband video signal of detected RF $x(t)$ with passband width B . The operators var and $\langle \cdot \rangle$ denote variance and expected value, respectively. If $x(t)$ is stationary, then $y(t)$ is stationary and the time dependence of the statistics is dropped. This simple model of the DD is valid if the detector's output video bandwidth is greater than or equal to the bandwidth B of the input.

An important property of ψ that it shares with β_2 is that it is constant under varying power of $x(t)$. If $x(t)$ is a band-limited Gaussian random process, then $y(t)$ is exponentially distributed (or chi-squared with two degrees of freedom) [11]. For exponential distributions, $\text{var}(y) = \langle y \rangle^2$ so that

$$\psi = 1. \quad (3)$$

The standard deviation of ψ can be shown as [4]

$$\text{NE}\Delta\psi = \sqrt{\frac{2}{B\tau}} \quad (4)$$

where τ is the integration time of the video amplifiers. The notation $\text{NE}\Delta\psi$ was chosen to be consistent with [10]. It also parallels the radiometric term Noise Equivalent Delta Temperature ($\text{NE}\Delta T$), which is the short-term standard deviation of a radiometer's output in kelvins.

B. Arbitrary Interferer

If an interferer with arbitrary amplitude modulation (AM) and phase modulation (PM) is introduced, then the input signal becomes

$$x(t) = a(t) \cos \omega t + b(t) \sin \omega t + A(t) \sin(\omega_c + \phi(t)) \quad (5)$$

which comprises natural thermal emission received by the antenna, self-generated receiver noise and interference. The natural emission and receiver noise are modeled by a band-limited zero-mean Gaussian random process centered at frequency ω with variance σ^2 . The interferer $A(t) \sin(\omega_c + \phi(t))$ can describe continuous wave (CW), AM, FM, PM, or pulsed signals. From (2), the pseudokurtosis is

$$\psi = 1 + \frac{\frac{1}{4}m_4 - \frac{1}{2}m_2^2}{\left(\frac{1}{2}m_2 + \sigma^2\right)^2} \quad (6)$$

where m_2 and m_4 represent the second and fourth raw moments of $A(t)$, respectively. The derivation is found in the Appendix.

Several properties of ψ under interference can be noted. First, if there is no interference, then ψ reduces to unity since $m_2 = m_4 = 0$. Second, ψ is only sensitive to the AM properties of the interference. Although it is certainly sensitive to PM and FM signals, it cannot distinguish them from CW. Finally, the ψ detector is "blind" to interferers with $m_4 = 2m_2^2$, as is the case when $A(t)$ is a Rayleigh process [9]. This is significant because fading due to moving stations is often well modeled by Rayleigh statistics and could potentially reduce the sensitivity of the system to interference.

The pseudokurtosis can be rewritten as a function of interference-to-noise ratio (INR) for specific classes of interferers. For example, the INR for CW (or PM or FM) signals is

$$\text{INR}(\text{CW}) = \frac{\frac{1}{2}A^2}{\sigma^2}. \quad (7)$$

For CW, $A(t) = A$ is a constant, $m_2(\text{CW}) = A^2$ and $m_4(\text{CW}) = A^4$; substituting these and (7) into (6) results in

$$\psi(\text{CW}) = 1 - \frac{\text{INR}^2}{(1 + \text{INR})^2}. \quad (8)$$

Pseudokurtosis is suppressed below unity for CW-type signals.

If the interferer is a pulsed sinusoid (e.g., radar), then $A(t)$ is the pulse envelope with duty cycle d and amplitude A , and

$$m_2(\text{pulse}) = \langle A^2(t) \rangle = A^2 d \quad (9)$$

$$m_4(\text{pulse}) = \langle A^4(t) \rangle = A^4 d \quad (10)$$

$$\text{INR}(\text{pulse}) = \frac{\frac{1}{2}A^2 d}{\sigma^2}. \quad (11)$$

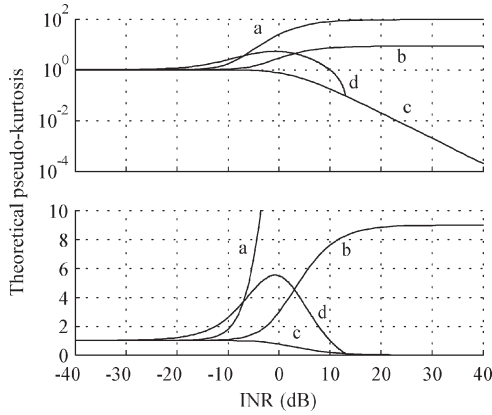


Fig. 2. Theoretical ψ versus INR for a pulsed sinusoid with (a) 1%, (b) 10% duty cycle, (c) CW, and (d) fixed amplitude with variable duty cycle. Both top and bottom plots show the same information but with different scales on the theoretical ψ axes.

Substituting (9)–(11) into (6) results in

$$\psi(\text{pulse}) = 1 + \frac{(1 - 2d)}{d} \frac{\text{INR}^2}{(1 + \text{INR})^2}. \quad (12)$$

For duty cycles less than 50%, ψ is greater than unity and can become quite large for very short duty cycles. As the duty cycle approaches 100%, ψ is reduced below unity and approaches the response to CW. If the duty cycle of the pulse is exactly 50%, then $\psi = 1$ and the interference goes undetected. This insensitivity to pulsed RFI with 50% duty cycle is also a characteristic of the true kurtosis [10].

Fig. 2 is a plot of theoretical ψ versus INR for continuous and pulsed sinusoidal RFI using (8) and (12), respectively. The upper panel shows ψ over six decades on log scale, and the lower panel shows a closer view on linear scale. Curve *a* has a fixed duty cycle of 1% with variable amplitude, whereas *b* has a fixed duty cycle of 10% with variable amplitude. Similar to the results in [10], there is a decrease in sensitivity of the system to pulsed RFI as the duty cycle increases from 1% to 10% as seen by curves *a* and *b*. Curve *c* is the theoretical ψ –INR response to CW. As the INR increases, the ψ reduces to zero in *c*. The response of ψ to fixed amplitude and variable duty cycle is examined in curve *d*. The ψ increases to a peak corresponding to a 4% duty cycle at an INR close to 0 dB and meets the CW curve when the duty cycle increases to 100%. The blind spot occurs at 50% duty cycle, which is 10-dB INR on the curve as it crosses the $\psi = 1$ value.

III. EXPERIMENTS

Two sets of experimental data were taken with the DD system: the DD in conjunction with an L-band zenith-viewing ground-based radiometer and a controlled laboratory experiment with CW RFI plus Gaussian noise input. A photograph of the DD hardware can be seen in Fig. 3. A 20-MHz bandwidth RF input is fed into a tunnel diode detector with more than 20 MHz of video bandwidth. A tunnel diode detector is used for its low output resistance and capacitance, allowing for a large video bandwidth. The video output is tapped off and amplified and integrated by a high input-impedance video

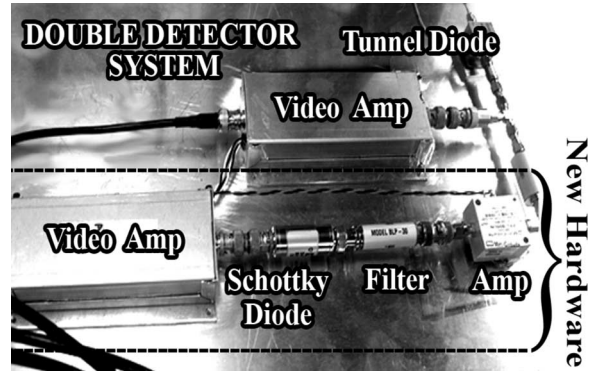


Fig. 3. Photograph of double-detector hardware.

amplifier with 125-kHz bandwidth to measure the second moment. As discussed later, the video amplifiers have shorter than normal integration time because the hardware was also used for pulse-blanking mitigation of radar interference. The detector and video amplifier above the horizontal line are typical of conventional radiometers. The DD is formed by adding the hardware below the line. The baseband VF signal from the first detector is amplified, detected, and integrated using a Schottky diode detector and second video amplifier. The Schottky diode detector was used for its low-end limit of 100 kHz on its input bandwidth.

A. Linearization

Practical low-noise receivers and microwave detectors suffer from inherent nonlinearity. The DD is no exception, and before it can be used to measure ψ and detect RFI, the nonlinearity must be characterized and removed. For the results in this paper, a polynomial expansion sufficiently describes the nonlinearity, and linearized ψ are presented for experimental data.

A constant gain or noise diode deflection method [12] is used to obtain the coefficients of the polynomial expansion for the first detector (or the second central moment). This is done by observing the noise diode deflections as the antenna noise temperature changes. The deflections are proportional to system gains at different operating points. Since linear systems must have constant gain, the ratio of any two deflections (or gains) should be unity. A ratio *D* is defined as

$$D_i = \frac{v_{1a_i} - v_{1an_i}}{v_{1a_0} - v_{1an_0}} \quad (13)$$

where the subscripts 0 and *i* indicate the reference and *i*th measurements, respectively; v_{1a_i} and v_{1a_0} are detector voltages while looking through the antenna; and v_{1an_i} and v_{1an_0} are detector voltages for antenna plus noise diode states. The reference measurements in the denominator should be made of a stable scene and often enough to eliminate thermal drifts in system gain. In practice, we used the sky scene approximately once over 30 s. The data used in (13) should also be free of interference. A system of linear equations is formed by substituting the linearizing formula for detector voltage, i.e.,

$$v_{\text{lin}} = v_1 + C_2 v_1^2 + \dots \quad (14)$$

into (13). The value v_{lin} is the corrected or linearized voltage of v_1 , which is the measured voltage output from the first detector, as indicated in Fig. 1, and is first corrected for dc offsets. The ratio D_i is computed for several values of v_{1a_i} and v_{1an_i} equated to one, and the unknown coefficients are obtained by least squares solution. Depending on the dynamic range of the system, the first detector output can be characterized by a second- or third-order polynomial, and a higher order polynomial is used to model the second detector output.

Forward models are then used to derive theoretical second- and pseudo-fourth-order moments, and thus, a nonlinear ψ , which is expressed by

$$\psi_{\text{nonlin}} = \frac{d_1 \text{var}(z) + d_2 (\text{var}(z))^2 + d_3 (\text{var}(z))^3 + \dots}{\langle z \rangle^2} \quad (15)$$

where z replaces y in Fig. 1 and is the modeled nonlinear output from the first microwave detector. For the second-order expansion in (14), this reduces to a function of v_{lin} and C_2 , which is shown as

$$\psi_{\text{nonlin}} = \frac{v_2}{v_1^2} = d_1 (1 + f_1(v_{\text{lin}}, C_2)) + d_2 f_2(v_{\text{lin}}, C_2) + d_3 f_3(v_{\text{lin}}, C_2) + \dots \quad (16)$$

where the only remaining unknowns are instrumental constants d_1 , d_2 , and d_3 . Note, d_1 is the DD system gain. The functions f are derived in the Appendix.

Antenna look data v_{1a} and v_{2a} are substituted into (16), and the remaining unknown instrumental constants are obtained by least squares solution. The antenna look data are used to estimate the instrumental constants since those data represent the expected operating dynamic range of the system. The resulting linearized ψ is

$$\psi_{\text{lin}} = \frac{\left(\frac{v_2}{v_1^2}\right) - d_2 f_2 - d_3 f_3 - \dots}{d_1} - f_1. \quad (17)$$

Finally, linearization constants can be estimated once and should remain valid, providing the system operating point (e.g., physical temperature) is constant.

B. Passive/Active L/S-Band Sensor (PALS) Radar/Radiometer

Over the course of two weeks in April and May 2006, the DD system was interfaced with the PALS Radar/Radiometer at the Jet Propulsion Laboratory (JPL) to collect field data.¹ This afforded the opportunity to test the system in a real RFI environment since PALS is susceptible to pulsed RFI from nearby airport radars. PALS operates in a three-position Dicke mode: cycling repeatedly between antenna only, antenna-plus-noise, and Dicke load positions. The DD received a 20-MHz bandwidth signal centered at 200 MHz from PALS. The DD integration time was set to 2 μs and the outputs sampled at 500 kHz. Approximately 1.5 TB of data was recorded and later

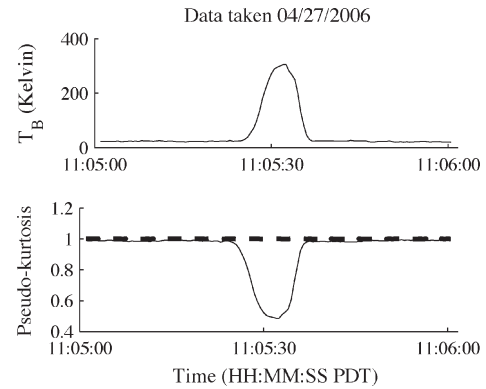


Fig. 4. Time series of (top panel) T_B and (solid line) nonlinear and (dashed line) linearized (bottom panel) ψ showing transitions from sky to ambient black body and back to sky. Note, the linearization process removes dependence of ψ upon T_B .

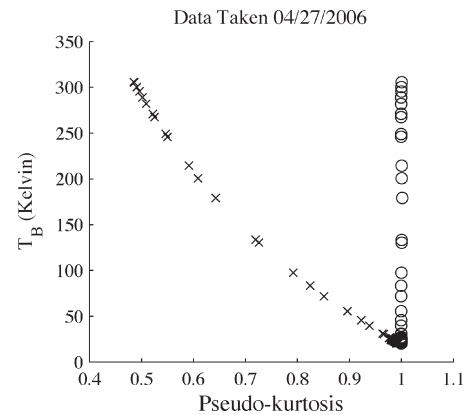


Fig. 5. Plot of antenna temperature versus (\times 's) nonlinear and (circles) linear pseudokurtosis using absorber test data.

linearized, calibrated² and reduced to 0.5-s integration time series of antenna temperature T_B and pseudokurtosis ψ .

The linearization process described in Section III-A was first applied to all 0.5-s integrated data. To collect the measurements needed to estimate the linearization constants, T_B was varied from cold sky to ambient blackbody temperature by slowly sliding microwave absorber over the aperture of the PALS antenna, which was pointed to zenith atop a building at JPL. Fig. 4 shows the time series of antenna temperature (top panel) and raw (solid line) and linearized (dashed line) ψ for the transition from sky to ambient blackbody and back to sky. Fig. 5 shows T_B versus raw (\times 's) and linearized (\circ 's) ψ for the same data set. To linearize ψ , the first and second detectors were modeled using second- and fourth-order polynomials, respectively. Note, the linearization process removes all dependence of ψ upon T_B , and the resulting linearized ψ values lie within a few $\text{NE}\Delta\psi$ about unity.

The results of a nightlong time series (from May 10 to May 11, 2006) of 0.5-s integrated data are shown in Fig. 6. The top panel shows calibrated T_B , and the bottom shows linearized ψ . The effects of RFI are clearly apparent in both

¹The JPL/PALS experiment also included participants and their RFI detection hardware from the University of Michigan and The Ohio State University.

²Data were calibrated assuming the PALS noise diode excess noise temperature was 500 K, and the front-end losses were 4.3 dB at a physical temperature of 33 $^\circ\text{C}$.

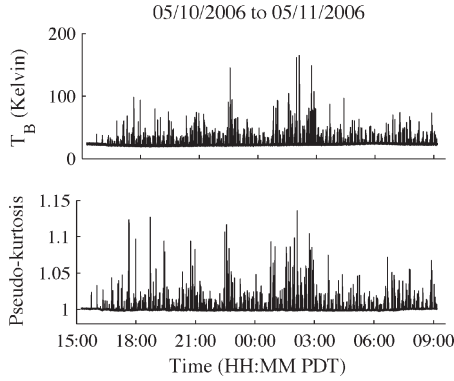


Fig. 6. Typical night-long time series.

T_B and ψ . Closer examination of the high-rate 500-kHz sampled time series revealed that the RFI was pulsed in nature and is likely due to local airport radars. The increase in ψ above unity is consistent with the presence of pulsed RFI, as expected from (12). This temporal correlation of increases in ψ with pulsed RFI in T_B is the first field validation of the DD.

To more closely examine the operation of the DD, a 4-min segment around 19:26 Pacific Daylight Time was chosen for further analysis. The antenna temperature and associated kurtosis time series of 0.5-s integrations are shown in Fig. 7. The pseudokurtosis time series were used to detect RFI, and detected events are indicated by the dots on the T_B curve. RFI was flagged if

$$|\psi - 1| > 4 \cdot \text{NE}\Delta\psi. \quad (18)$$

As can be seen in Fig. 7, strong RFI events of tens of kelvins are accompanied by obvious amounts of excess ψ . Several smaller events, not so obviously RFI, were also detected by small fluctuations in ψ of only a few $\text{NE}\Delta\psi$. A total of 30 RFI events were flagged over the 4-min period. The flagged data can be dropped from the observations resulting in an “RFI-free” time series.

To validate the DD detection methodology, a conventional pulse-detection and blanking algorithm similar to that used in [1] was applied to the 500-kHz sampled data before 0.5-s integration. According to [1], such an algorithm was highly effective for mitigation against radar interference in radio telescopes. For each 0.5-s integration, there are approximately 83 000 antenna-only samples and antenna-plus-noise samples each. A threshold level is set for these populations, and any 2- μs sample greater than the limit are removed. The threshold for each window is determined by its mean $m(t)$ and standard deviation $\sigma(t)$ without the largest 10% of samples, resulting in a detection when

$$v_1(t) - m(t) > 7\sigma(t). \quad (19)$$

The remaining samples are integrated to form the 0.5-s measurements.

Fig. 8 shows the two mitigated T_B time series and their difference. The top series is the raw T_B with ψ -flagged RFI simply removed (as evidenced by gaps in the curve). The 30 RFI

flags are shown as + symbols. The middle series is the pulse-blanked T_B , which we take as “ground truth” for validation purposes. The pulse-detection algorithm produced 59 RFI flags, also shown as + symbols. Of the 30 ψ -based flags, the pulse-detection algorithm flagged 29. It also flagged an additional 30 events not detected by the ψ algorithm. The difference in the two mitigated T_B series is shown at the bottom. The dash-dot line on the same plot is at $\text{NE}\Delta T$ and indicates that the RFI events missed by ψ detection were typically $\lesssim 2 \text{ NE}\Delta T$ in size, with one event $\sim 4 \text{ NE}\Delta T$ in size. Such a detection threshold is consistent with the digital kurtosis detector of Ruf *et al.* [10]. Thus, the DD captured RFI events down to a level approximately two to four times $\text{NE}\Delta T$.

C. Gaussian Plus CW Experiment

A laboratory experiment was designed to quantitatively compare measured and theoretical responses of the DD to CW RFI. A Gaussian input was created by a noise source which varied from about -33 to -25 dBm in 1-dB steps. A second noise source was coupled in and switched on and off to provide data for linearization. Thus, the two noise sources simulate RFI-free antenna and antenna-plus-noise radiometer states. As was previously done, second- and fourth-order polynomials were used to model the first and second detectors, respectively. RFI was added using an in-band sinusoid that varied from -64 to -34 dBm for each noise power increment producing INRs ranging from -40 to 0 dB. Video amplifier null offsets were measured by switching the first detector’s input to a load.

A plot of the measured and linearized ψ versus INR is shown in Fig. 9 along with the theoretical ψ -INR curve from (8). The laboratory data closely follow the theoretical curve for low INR values up to about -15 dB. For higher values, ψ depresses below unity, as predicted by (8). There is a slight bias in the plot above -15 dB INR. This occurs because the linearization process is carried out using data taken with only Gaussian input, and the introduction of an interferer compromises the linearization of the detectors [7]. Additionally, certain INR values could not be covered (seen in Fig. 9 as missing \times ’s) due to the limitations of the experimental design. The missing INR values correspond to power levels that were above the range used to linearize the detectors. The linearization polynomials were not valid for these corresponding high input powers. With these constraints on the quantitative experiment in mind, the experimental data quite satisfactorily follow the theory.

IV. DISCUSSION

Hardware and agreement with the theory of a DD for RFI detection in microwave radiometers was demonstrated. The detector is based on the principle of using kurtosis to detect the presence of non-Gaussian signals. It was shown that the DD approximates the kurtosis. Behavior of this pseudokurtosis measured in the presence of CW and pulsed RFI was derived and tested in two experiments. A controlled laboratory experiment shows a good quantitative agreement between the theory and

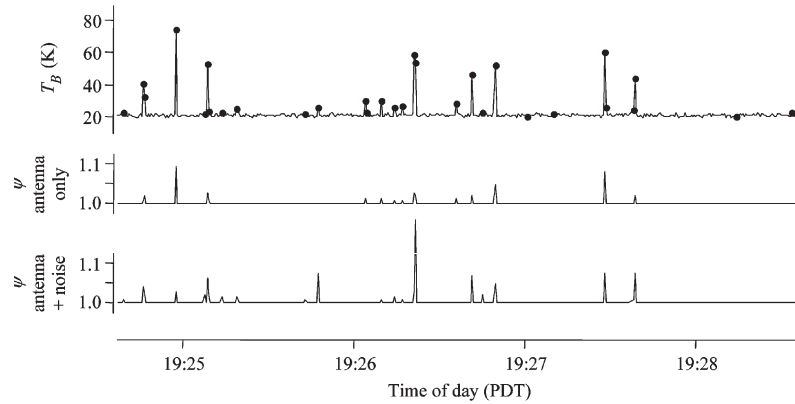


Fig. 7. RFI events detected by pseudokurtosis as indicated by dots on the T_B time series (top). The middle and bottom plots are the pseudokurtosis time series for the two radiometer states viewing the antenna (antenna only and antenna-plus-noise, respectively).

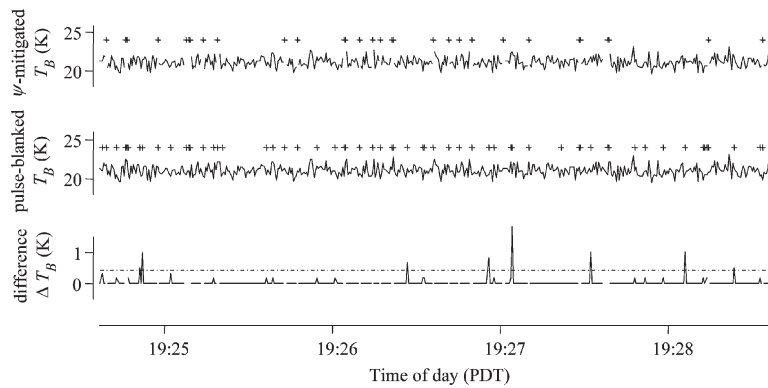


Fig. 8. Mitigated T_B time series using (top) ψ and (middle) pulse-blanking. The bottom curve shows the difference between the two with $NE\Delta T$ marked with a dash-dot line.

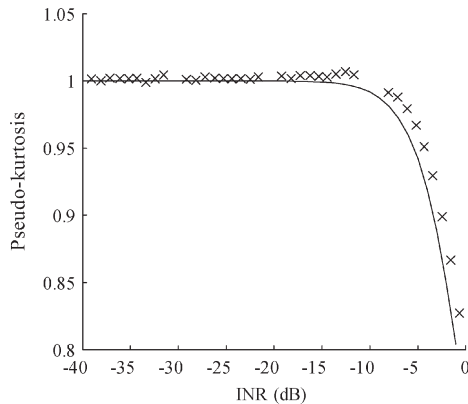


Fig. 9. Plot of laboratory data showing ψ versus INR (\times 's) along with the theoretical response (solid line).

experiment for a wide range of INRs. A field experiment using a ground-based radiometer in the presence of radar interference showed that the DD was sensitive to pulsed RFI, as low as approximately twice the $NE\Delta T$. The pseudokurtosis measured by the detector exhibited the expected behavior in both cases. The hardware implementation of the DD was quite simple, using two microwave detectors, a wideband amplifier, and two video amplifier-integrators. This technique is quite compatible with the existing direct-detection radiometer designs and uses basic microwave and analog circuit components, both of which are desirable for applications requiring low technological risk.

APPENDIX

A. Response to Interference

The appendix contains further amplification on the mathematical operations carried out by the hardware shown in the block diagram in Fig. 1. The DD response to an interferer in the presence of Gaussian noise was given in (6). The input to the first detector is

$$x(t) = a(t) \cos \omega t + b(t) \sin \omega t + A(t) \sin(\omega_c t + \phi(t)) \quad (20)$$

where the band-limited Gaussian random process is represented by its in and quadrature-phase components a and b , respectively. The VF process $y(t)$, as shown in the following equation, is found by taking the baseband components of $x^2(t)$ (as indicated by the LPF operator in Fig. 1):

$$y(t) = \frac{1}{2}A(t)^2 + \frac{1}{2}a(t)^2 + \frac{1}{2}b(t)^2 + A(t)a(t) \cos(\phi(t) + (\omega_c - \omega)t) + A(t)b(t) \sin(\phi(t) + (\omega_c - \omega)t). \quad (21)$$

Note, if the frequency difference between the radiometer band center ω and the RFI carrier frequency ω_c is larger than the video bandwidth of the detector, the last two terms of (21) will not appear in the detector VF output, and thus not be measured by the second detector. Likewise, we assume the bandwidth of the interferer is less than the video bandwidth of the first

detector. To find ψ , the mean and variance of $y(t)$ need to be computed. Because $a(t)$ and $b(t)$ are zero-mean random processes independent of $A(t)$ and $\phi(t)$, the last two terms of $y(t)$ are also zero mean. Thus, the mean of $y(t)$ is

$$\begin{aligned}\langle y(t) \rangle &= \frac{1}{2} \langle A(t)^2 \rangle + \frac{1}{2} \langle a(t)^2 \rangle + \frac{1}{2} \langle b(t)^2 \rangle \\ &= \sigma^2 + \frac{1}{2} m_2\end{aligned}\quad (22)$$

where σ^2 is the variance of the input Gaussian random process contained in $x(t)$. From the radiometer's point of view, the AM information of RFI $A(t)$ can be treated as a quasi-stationary random process (at least over the radiometer integration time), and m_2 is the conventional second raw moment of $A(t)$. Thus, the mean of the first detector's output is the sum of the Gaussian noise and interferer signal power.

The variance is computed by

$$\text{var}(y(t)) = \langle y(t)^2 \rangle - \langle y(t) \rangle^2. \quad (23)$$

The first term is

$$\begin{aligned}\langle y^2 \rangle &= \langle A^2 \rangle \langle a^2 \rangle + \langle A^2 \rangle \langle b^2 \rangle + \frac{1}{2} \langle a^2 \rangle \langle b^2 \rangle \\ &\quad + \frac{1}{4} \langle A^4 \rangle + \frac{1}{4} \langle a^4 \rangle + \frac{1}{4} \langle b^4 \rangle\end{aligned}\quad (24)$$

where the time dependence has been dropped by stationarity. The fourth moment of a and b terms is equal to $3\sigma^2$ [9]. Thus

$$\langle y^2 \rangle = 2\sigma^4 + \frac{1}{4} m_4 + 2m_2\sigma^2 \quad (25)$$

where m_4 is the fourth raw moment of $A(t)$. The variance is then

$$\begin{aligned}\text{var}(y(t)) &= 2\sigma^4 + \frac{1}{4} m_4 + 2m_2\sigma^2 - \left(\sigma^2 + \frac{1}{2} m_2 \right)^2 \\ &= \sigma^4 + \frac{1}{4} m_4 + \sigma^2 m_2 - \frac{1}{4} m_2^2.\end{aligned}\quad (26)$$

Finally, by definition (2)

$$\begin{aligned}\psi &= \frac{\sigma^4 + \frac{1}{4} m_4 + \sigma^2 m_2 - \frac{1}{4} m_2^2}{\left(\sigma^2 + \frac{1}{2} m_2 \right)^2} \\ &= 1 + \frac{\frac{1}{4} m_4 - \frac{1}{2} m_2^2}{\left(\sigma^2 + \frac{1}{2} m_2 \right)^2}\end{aligned}\quad (27)$$

which is (6).

A. Linearization

The nonlinear model of the DD is presented in this section. The input signal without RFI to the first detector is

$$x(t) = a(t) \cos \omega t + b(t) \sin \omega t. \quad (28)$$

The output of the first detector is found by taking the baseband components of a power series of the input as

$$z = \text{LPF} \left(\sum_{n=0}^{\infty} c_n x^n \right). \quad (29)$$

The LPF operator is an ideal LPF with cutoff frequency above the detector's video bandwidth and below ω . We assume ω to be much larger than the detector video bandwidth, so that [7]

$$z = c_0 + \frac{1}{2} a^2 c_2 + \frac{1}{2} b^2 c_2 + \frac{3}{8} a^4 c_4 + \frac{3}{8} b^4 c_4 + \frac{3}{4} a^2 b^2 c_4 + \dots \quad (30)$$

Note, in an ideal detector, only the c_2 coefficient is nonzero and is commonly referred to as the detector sensitivity. The process $y(t)$ in Section II-A contains only the terms with the c_2 coefficients.

The first video amplifier provides additional gain g_1 and averaging as indicated by the expected-value operator $\langle \cdot \rangle$ in the following equation:

$$\begin{aligned}v_1 &= g_1 \langle z \rangle \\ &= g_1 (c_2 P_x + 3c_4 P_x^2)\end{aligned}\quad (31)$$

where P_x is the power (in a 1- Ω system) of the input signal x , and g_1 is the video amplifier gain. Any null offset value is assumed removed. To linearize the detector, the linear term is sought from v_1 . Hence

$$\begin{aligned}v_{\text{lin}} &\equiv g_1 c_2 P_x \\ &= v_1 + C_2 v_1^2\end{aligned}\quad (32)$$

where

$$C_2 = \frac{-3c_4}{g_1 c_2^2}. \quad (33)$$

The C_2 coefficient is found using the deflection ratio linearization process [12].

The second detector measures the power or variance of the output from the first by

$$\text{var}\{z\} = c_2^2 P_x^2 + 12c_2 c_4 P_x^3 + 45c_4^2 P_x^4. \quad (34)$$

If the second detector is likewise modeled by a power series, then the output of the second video amplifier with gain g_2 and null offset removed is

$$\begin{aligned}v_2 &= g_2 \left(d_1 \text{var}\{z\} + d_2 (\text{var}\{z\})^2 \right. \\ &\quad \left. + d_3 (\text{var}\{z\})^3 + d_4 (\text{var}\{z\})^4 + \dots \right).\end{aligned}\quad (35)$$

The nonlinear ψ is defined as

$$\psi_{\text{nonlin}} = \frac{v_2}{v_1^2}. \quad (36)$$

After substituting (31)–(35) into (36), and applying a bit of rearranging, the ratio can be written as

$$\begin{aligned}\psi_{\text{nonlin}} &= d_1 \frac{g_2}{g_1^2} \left(1 + \frac{-2C_2 v_{\text{lin}} + 4C_2^2 v_{\text{lin}}^2}{1 - 2C_2 v_{\text{lin}} + C_2^2 v_{\text{lin}}^2} \right) \\ &\quad + d_2 \frac{g_2}{g_1^4} \frac{(v_{\text{lin}}^2 (1 - 4C_2 v_{\text{lin}} + 5C_2^2 v_{\text{lin}}^2))^2}{v_{\text{lin}}^2 (1 - 2C_2 v_{\text{lin}} + C_2^2 v_{\text{lin}}^2)} \\ &\quad + d_3 \frac{g_2}{g_1^6} \frac{(v_{\text{lin}}^2 (1 - 4C_2 v_{\text{lin}} + 5C_2^2 v_{\text{lin}}^2))^3}{v_{\text{lin}}^2 (1 - 2C_2 v_{\text{lin}} + C_2^2 v_{\text{lin}}^2)} + \dots\end{aligned}\quad (37)$$

Or, subsuming the video amplifier gains into the polynomial coefficients, the following is derived:

$$\psi_{\text{nonlin}} = d_1 (1 + f_1(v_{\text{lin}}, C_2)) + d_2 f_2(v_{\text{lin}}, C_2) + d_3 f_3(v_{\text{lin}}, C_2) + \dots \quad (38)$$

Finally, the linearized pseudokurtosis is then found as

$$\psi_{\text{lin}} = \frac{\left(\frac{v_2^2}{v_1^2} - d_2 f_2 - d_3 f_3\right)}{d_1} - f_1. \quad (39)$$

ACKNOWLEDGMENT

The authors would like to thank S. Yueh and S. Dinardo of the Jet Propulsion Laboratory for use and support of the PALS radiometer; J. Lucey of NASA's Goddard Space Flight Center for providing excellent field support during the experiment; and C. Ruf (University of Michigan) and J. Johnson (The Ohio State University) for the many useful discussions about RFI detection and mitigation.

REFERENCES

- [1] S. W. Ellingson and G. A. Hampson, "Mitigation of radar interference in L-band radio astronomy," *Astrophys. J., Suppl. Ser.*, vol. 147, no. 1, pp. 167–176, Jul. 2003.
- [2] S. W. Ellingson and J. T. Johnson, "A polarimetric survey of radio-frequency interference in C- and X-bands in the continental United States using WindSat radiometry," *IEEE Trans. Geosci. Remote Sens.*, vol. 44, no. 3, pp. 540–548, Mar. 2006.
- [3] J. T. Johnson, A. J. Gasiewski, B. Guner, G. A. Hampson, S. W. Ellingson, R. Krishnamachari, N. Niamsuwan, E. McIntyre, M. Klein, and V. Y. Leuski, "Airborne radio-frequency interference studies at C-band using a digital receiver," *IEEE Trans. Geosci. Remote Sens.*, vol. 44, pt. 2, no. 7, pp. 1974–1985, Jul. 2006.
- [4] J. F. Kenney and E. S. Keeping, "Kurtosis," in *Mathematics of Statistics*, 3rd ed. Princeton, NJ: Van Nostrand, 1962, ch. 1, pp. 102–103.
- [5] D. M. LeVine and S. Abraham, "Galactic noise and passive microwave remote sensing from space at L-band," *IEEE Trans. Geosci. Remote Sens.*, vol. 42, no. 1, pp. 119–129, Jan. 2004.
- [6] L. Li, P. W. Gaiser, M. H. Bettenhausen, and W. Johnston, "WindSat radio-frequency interference signature and its identification over land and ocean," *IEEE Trans. Geosci. Remote Sens.*, vol. 44, no. 3, pp. 530–539, Mar. 2006.
- [7] T. Närhi, "Nonlinearity characterisation of microwave detectors for radiometer applications," *Electron. Lett.*, vol. 32, no. 3, pp. 224–225, Feb. 1996.
- [8] E. Njoku, P. Ashcroft, T. Chan, and L. Li, "Global survey and statistics of radio-frequency interference in AMSR-E land observations," *IEEE Trans. Geosci. Remote Sens.*, vol. 43, no. 5, pp. 938–947, May 2005.
- [9] A. Papoulis, *Probability Random Variables, and Stochastic Processes*, 3rd ed. New York: McGraw-Hill, 1991, pp. 109–111.
- [10] C. Ruf, S. Gross, and S. Misra, "RFI detection and mitigation for microwave radiometry with an agile digital detector," *IEEE Trans. Geosci. Remote Sens.*, vol. 44, no. 3, pp. 694–706, Mar. 2006.
- [11] F. Ulaby, R. Moore, and A. Fung, *Microwave Remote Sensing: Active and Passive. Vol. 2. Radar Remote Sensing and Surface Scattering and Emission Theory*. Norwood, MA: Artech House, 1986, ch. 7-2, pp. 463–494.
- [12] W. J. Wilson, A. B. Tanner, F. A. Pellerano, and K. A. Horgan, "Ultra stable microwave radiometers for future sea surface salinity missions," JPL Rep. D-31794, Apr. 2005. Instrument Incubator Program Final Report.



Jeffrey R. Piepmeier (S'93–M'99) received the B.S. degree in engineering from LeTourneau University, Longview, TX, in 1993 and the M.S. and Ph.D. degrees in electrical engineering from the Georgia Institute of Technology, Atlanta, in 1999 and 1994, respectively.

From 1993 to 1994, he was a Schakleford Fellow with the Georgia Tech Research Institute. In 1999, he joined the Microwave Instrument Technology Branch, NASA's Goddard Space Flight Center, Greenbelt, MD, as a Principal Investigator on several technology development projects in microwave radiometry. During 2004–2005, he led the Hydros radiometer team. He is currently a Calibration Lead for the NASA Aquarius radiometer.

Dr. Piepmeier is a member of the Union Radio Scientifique Internationale Commission F and the American Geophysical Union. He is a past Chair of the Geoscience and Remote Sensing Society Instrumentation and Future Technologies technical subcommittee and a 2002 NASA Earth Science New Investigator. He is currently a Vice-Chair of the National Academies' Committee on Radio Frequencies (CORF). He received the third place in the 1998 IGARSS student prize paper competition. He was a recipient of an Excellence in Federal Career Gold Award (Rookie-of-the-year) in 2000. He was a Chair of the 2000 Microwave Radiometer Calibration Workshop (MicroCal2000). He was the recipient of the NASA/GSFC Exceptional Achievement Award and Technology Advancement Award in 2005 and 2007, respectively.



Priscilla N. Mohammed (S'02–M'06) received the B.S. degree in electrical engineering from the Florida Institute of Technology, Melbourne, in 1999 and the M.S. and Ph.D. degrees in electrical engineering from the Georgia Institute of Technology, Atlanta, in 2001 and 2005, respectively.

As a Ph.D. student, she performed microwave measurements of gaseous phosphine and ammonia under simulated conditions for the outer planets and used these measurements to develop a radio occultation simulator to predict absorption and excess Doppler due to Saturn's atmosphere. Much of this work was in support of the Cassini mission to Saturn. Based on these laboratory results, the Cassini Project Science Group made the decision to extend the Ka-band (32 GHz) operation throughout the mission tour. The predicted attenuation profiles for the Cassini radio occultation maneuver of May 2005 earned her an invitation from the Cassini Radio Science Team to present a paper on their behalf at the 37th Annual Meeting of the Division for Planetary Sciences in Cambridge, U.K. In 2006, she joined the Goddard Earth Sciences and Technology Center with the University of Maryland Baltimore County, Baltimore as a member of the research faculty. She is also with the Microwave Instrument Technology Branch at NASA's Goddard Space Flight Center, Greenbelt, MD. Her current research interests include radio frequency interference mitigation in microwave radiometers.



Joseph J. Knuble received the B.S. degree in electrical and computer engineering from Worcester Polytechnic Institute, Worcester, MA, in 2002 and the M.S. degree in electrical and computer engineering from Johns Hopkins University, Baltimore, MD, in 2007.

In 2002, he joined the Microwave Instrument Technology Branch, NASA's Goddard Space Flight Center, Greenbelt, MD, where he worked on airborne and spaceflight radiometers and radars. He is currently doing various microwave research projects, in

addition to support for the NASA Aquarius radiometer.

Mr. Knuble received a NASA Special Act Award in 2003 for recognition of optimal phase-noise reduction in distributed phase-locked oscillators for STAR receiver LOs.